Impact of igneous intrusion and associated ground deformation on the stratigraphic record

Emilia M. Dobb[1], Craig Magee[2]*, Christopher A.-L. Jackson[1,3], Bailey Lathrop[1], Jonas Köpping[4]

[1]Basins Research Group (BRG), Department of Earth Science and Engineering, Royal School of Mines, Prince Consort Road, Imperial College London, SW7 2BP, England, UK.
[2]School of Earth and Environment, University of Leeds, Leeds, LS2 9JT, UK.
[3]present address: Department of Earth and Environmental Sciences, University of Manchester, Williamson Building, Oxford Road, Manchester, M13 9PL, UK
[4]School of Earth, Atmosphere and Environment, Monash University, Melbourne, 3800, Australia

*Correspondence (c.magee@leeds.ac.uk)

Abstract

The geomorphology and sediment systems of volcanic areas can be influenced by uplift (forced folding) related to subsurface migration and accumulation of magma. Seismic geomorphological analysis presents a unique tool to study how surface morphology and subsurface magma dynamics relate, given seismic reflection data can image buried landscapes and underlying intrusions in 3D at resolutions of only a few metres-to-decametres. However, differential compaction of the sedimentary sequence above incompressible igneous intrusions during burial modifies palaeosurface morphology. Here we use 3D seismic reflection data from offshore NW Australia to explore how the stratigraphic record of igneous

intrusion and associated ground deformation can be unravelled. We focus on a forced fold that formed in the Early Cretaceous to accommodate intrusion of magma, but which was later amplified by burial-related differential compaction of the host sedimentary sequence. We show how: (1) marine channels and clinoforms may be deflected by syn-depositional intrusion-induced forced folds; and (2) differential compaction can locally change clinoform depth post-deposition, potentially leading to erroneous interpretation of shoreline trajectories. Our results demonstrate seismic geomorphological analysis can help us better understand how magma emplacement translates into ground deformation, and how this shapes the landform of volcanic regions.

Introduction

The development of volcanic landforms modifies Earth surface processes (e.g., Karlstrom et al. 2018). For example, in addition to the construction of volcanoes through the eruption of lava, subsurface magma emplacement and accumulation can create dome-like relief by uplifting the overlying rock and free surface, producing a forced fold (e.g., van Wyk de Vries et al. 2014; Magee et al. 2017b). Most studies of ancient and active forced folds use the relationship between fold and intrusion geometry to unravel the kinematics and dynamics of magma emplacement (e.g., Pollard & Johnson 1973; Jackson & Pollard 1990; Hansen & Cartwright 2006; Reeves et al. 2018); this is critical to volcano monitoring and hazard mitigation, given we can invert intrusion-induced ground deformation to locate and track intruding magma volumes (Galland & Scheibert 2013; Segall 2013). We also recognise that the production of surface relief through intrusion-induced forced folding can modify sediment dispersal, although few studies have explored this in detail (e.g., Smallwood & Maresh 2002; Egbeni et al. 2014; Magee et al. 2014; Magee et al. 2017a). Deciphering precisely how changes in geomorphology relate to magma plumbing system dynamics is also critical to volcanic hazard assessment (e.g., van Wyk de Vries et al. 2014; Karlstrom et al. 2018). Seismic geomorphological analysis potentially provides a powerful tool for exploring the interaction between palaeosurface deformation, sediment systems, and magmatism, but we have to be aware that burial-related differential compaction may modify and obscure the stratigraphic record of these processes (e.g., Magee et al. 2019).

Here, we use 3D seismic reflection and borehole data from the Exmouth Plateau, offshore NW Australia (Fig. 1A), to examine the formation of a forced fold above a laccolith and its influence on the stratigraphic record of the overlying Barrow Group. We use seismic-stratigraphic relationships (e.g., onlap, erosional truncation) to determine a likely Early Cretaceous (Berriasian) age for intrusion. We show that marine channels and clinoforms forming part of the Early Cretaceous Barrow Group were locally deflected around and onlap onto the forced fold; these observations build on previous studies demonstrating that intrusion-induced forced folds can control sediment dispersal (e.g., Smallwood & Maresh 2002; Magee et al. 2014; Magee et al. 2017a). We also show that burial-related differential compaction modified the stratigraphic record of the area post-intrusion, causing clinoform inflection points to appear locally elevated across the forced fold. If not recognised, this change in the elevation of clinoform inflection points, driven by differential compaction, may be misinterpreted as evidence of relative sea-level change. Our results highlight seismic geomorphology is an important tool for understanding interactions between intrusion-induced ground deformation, landscape development, and sediment dispersal in volcanic regions, but that we need to account for burial-related compaction.

Geological Setting

The Exmouth Plateau is part of the North Carnarvon Basin, offshore NW Australia. The plateau covers ~300,000 km^2, occurs at a depth of 0.8–4 km below the sea surface, and comprises <10 km thick crystalline overlain by an up to 18 km thick sequence of sedimentary rock (Fig. 1) (Willcox & Exon 1976; Exon et al. 1992; Longley et al. 2002; Stagg et al. 2004; Direen et al. 2008). The North Carnarvon Basin formed through multiple phases of extension between the Late Carboniferous and Early Cretaceous, as Australia and Greater India rifted apart (Exon et al. 1982; Longley et al. 2002; Stagg et al. 2004). Rifting in the Late Triassic-to-Early Jurassic and Late Jurassic-to-Early Cretaceous was accommodated by the formation of normal faults that: (i) offset the dominantly fluvio-deltaic, siliciclastic pre-rift succession of the Triassic Locker Shale and Mungaroo Formation; and (ii) accommodated a thin siliciclastic sequence of Jurassic shallow marine sandstones and siltstones (e.g., Brigadier Formation) and the deep marine Dingo Claystone (Figs 1B and C) (Willcox & Exon 1976; Tindale et al. 1998; Stagg et al. 2004; Bilal et al. 2018). During the final phases of rifting, regional uplift and development of the Base Cretaceous unconformity preceded rapid subsidence and the deposition of the northwards prograding Barrow Group (Figs 1B and C) (Reeve et al. 2016; Paumard et al. 2018). Clinoforms within the Barrow Group are ~100–550 m high and have slopes of 1–9º, indicating they define a long, linear, ramp-like shelf-margin, rather than a discrete delta (e.g., Fig. 1C) (Paumard et al. 2018). The top of the Barrow Group is marked by a regional unconformity, which is capped by the Zeepaard Formation and Birdrong Sandstone (Fig. 1B) (Reeve et al. 2016). Rifting ceased in the Early Cretaceous, associated with the breakup of Australia and Greater India, leading to thermal subsidence and development of a post-rift passive margin (Fig. 1B) (Stagg et al. 2004; Gibbons et al. 2012). This transition to a passive margin was marked by the onset of deposition of the deep marine Muderong Shale, within which a polygonal fault tier subsequently formed (Fig. 1B) (Tindale et al. 1998).

Magmatism in the North Carnarvon Basin occurred periodically throughout the Middle Jurassic-to-Early Cretaceous (Fig. 1B). A seismically high-velocity (~6.2–7.4 km s^{-1})

body within the lower crust of the Exmouth Plateau is interpreted as a large magmatic body, likely of mafic-to-ultramafic composition, emplaced during the Callovian (Fig. 1B) (Frey et al. 1998; Rey et al. 2008; Rohrman 2013, 2015). Spatially if perhaps not genetically associated with this high-velocity body are: (i) a radial dyke swarm (the Exmouth Dyke Swarm), which was emplaced at ~148 Ma (Tithonian) (Magee & Jackson 2020); and (ii) a series of sills and sill-complexes, which seismic-stratigraphic dating of intrusion-induced forced folds suggests were emplaced in the Kimmeridgian and Berriasian-to-Valanginian (Figs 1B and C) (Symonds et al. 1998; Magee et al. 2013b; Magee et al. 2013a; Magee et al. 2017a; Mark et al. 2020; Norcliffe et al. 2021). The final phase of igneous activity coincided with continental break-up and the development of a continent-ocean transition zone outboard of the Exmouth Plateau (Figs 1A and B) (Hopper et al. 1992; Direen et al. 2008; Reeve et al. 2021).

Dataset and Methods

Data

We use the Glencoe dataset, which is a zero-phase, time-migrated, 3D seismic reflection survey (Figs 1A and 2). The survey covers an area of ~4042 km^2, has a line spacing of 25 m, recorded to a depth of ~8 s two-way time (TWT), and is displayed with SEG (Society for Exploration Geophysicists) positive polarity; i.e. a downward increase in acoustic impedance correlates with a peak (red-yellow reflection), and a downward decrease in acoustic impedance correlates with a trough (blue reflection). We map the upper and lower contacts of the studied intrusion, as well as one horizon beneath it (the Top Mungaroo Formation), and five horizons above; borehole data from the nearby Chester-1ST1 borehole allow us to identify the lithology and age of the sedimentary sequences containing these horizons (Fig. 2). To tie the well and seismic reflection data we create a synthetic seismogram using

Chester-1ST1 well-log (density and sonic velocity) and checkshot information from a depth range of ~2.3–4.5 km TVD (true vertical depth) (Fig. 2C).

No boreholes intersect the intrusion or fold studied here, so we cannot directly constrain their composition or physical properties (e.g., seismic velocity) (Fig. 2A). Due to this lack of borehole data, and because the possible seismic velocity range (4.0–7.5 km s^{-1}) of igneous intrusions is rather large (see Magee et al. 2015 and references therein), we do not depth-convert the seismic reflection data. Instead, we depth-convert measurements in seconds TWT for the intrusion and folded sedimentary sequence using: (i) seismic velocities of ~5.55 (±10%) km s^{-1} for the intrusion, which marks the typical range of mafic igneous rocks (Skogly 1998; Planke et al. 2005) similar to the basaltic sill and dyke penetrated in the nearby Rimfire-1 and Chester-1ST1 boreholes (Fig. 2A) (Moig N & Massie 2010; Childs et al. 2013); and (ii) the time-depth relationship for the sedimentary sequence determined from the checkshot data for nearby boreholes (i.e. Briseis-1, Chester-1ST1, Glencoe-1, Nimblefoot-1, and Warrior-1; Fig. 2A), which indicates the Barrow Group and the underlying folded sequence has an interval velocity of ~3.0 (±0.5) km s^{-1} (Supplementary Figure 1; Supplementary Table 1). These seismic velocity ranges, coupled with measurements of dominant frequency, also allow us to estimate the data resolution. We define the limit of separability ($\lambda/4$, where λ is the dominant wavelength), i.e. the minimum vertical distance between two boundaries required to produce two distinct reflections, and the limit of visibility ($\lambda/30$) below which reflections cannot be distinguished from noise (Brown 2011). If the vertical distance between boundaries is less than the limit of separability, but greater than the limit of visibility, the reflections from these boundaries will merge on their return to the surface and cannot be deconvolved, producing a tuned reflection package rather than two distinct reflections (Widess 1973; Brown 2011). The dominant frequency of the data in the study area is ~25 Hz, indicating the limit of separability is ~56 (±6) m and the limit of visibility is ~7 (±1) m for the intrusion (Norcliffe et al. 2021). For the Barrow Group and folded sequence, the limits of separability and visibility are ~30 (±5) m and ~4 (±1) m, respectively. The horizontal resolution of the time-migrated seismic reflection data is likely up to ~30 (±5) m (i.e. λ/4).

Results

Intrusion seismic expression, geometry, and stratigraphic context

The intrusion is elliptical, elongated NE, ~4.5 km long, and can be sub-divided into two components: (i) a tabular, strata-concordant main body (3.9 × 2.5 km) that on average is ~104 ms TWT thick (~260–317 m assuming a velocity of ~5.55 (±10%) km s^{-1}), but which is locally up to ~202 ms TWT thick (~504–617 m); and (ii) encompassing inclined sheets, expressed as tuned reflection packages, which transgress upwards from (up to ~180 ms TWT or ~225–315 m high) and dip in towards the main body (Figs 2B, C, and 3). The intrusion occurs within a NE-trending graben and is encased by Late Triassic-to-Jurassic strata (Figs 2B and C). Both the top and base contacts of the intrusions main body are resolved, with the Top Intrusion contact corresponding to a high amplitude, continuous, positive polarity reflection (Fig. 2B and C). The Base Intrusion contact corresponds to a moderate-to-high amplitude, negative polarity reflection that broadly coincides with the Top Mungaroo Formation (Figs 2B and C). There is an up to ~57 ms TWT (~71–100 m) high, NE-trending ridge along the centre of the main intrusion, with the Top Intrusion contact lower on its western side, (Fig. 3A); the ridge is not seen on the Base Intrusion contact (Fig. 3B).

Stratigraphic and structural framework

The Top Mungaroo Formation is expressed as a high amplitude, negative polarity reflection that is offset by planar and arcuate, ~NE-SW striking normal faults (purple horizon in Fig. 2);

this overall structural framework is mirrored by the shallower Near Base Cretaceous unconformity (Fig. 4A), which is expressed as a moderate-to-high amplitude, positive polarity reflection (Figs 2B and C). Unlike the Top Mungaroo Formation, the Near Base Cretaceous unconformity is locally uplifted by up to ~200 ms TWT (~250–350 m) directly above the intrusion, relative to its regional trend (blue horizon in Figs 2B, C, and 4A). This uplift of the Near Base Cretaceous unconformity occurs at an abrupt offset, i.e. an annular vertical fault, coincident with the lateral edge of the intrusion (Figs 2B, C, and 4A). Within the uplifted section of the Near Base Cretaceous unconformity, a narrow graben bound by NE-SW striking normal faults with throws of ≲60 ms TWT (≲75–105 m) is present, along with several minor intra-graben faults (Figs 2B, C, and 4A). These NE-SW striking faults extend down to the ridge expressed along the Top Intrusion contact, and are broadly parallel to but are physically separate from, those outside the area of uplift (Figs 2B, C, and 4A).

Above the Near Base Cretaceous unconformity, the Intra-Barrow Group 1 horizon also displays an area of uplift above the intrusion but there is less evidence of faulting across its extent, although its lack of lateral continuity means it can only be locally mapped (green dashed horizon in Figs 2B, C, and 4B); the horizon onlaps onto an underlying reflection before reaching the Chester-1ST1 borehole, such that we cannot determine its absolute age (Fig. 2C). In contrast to the abrupt uplift of the Near Base Cretaceous unconformity across an sub-vertical, annular fault, the Intra-Barrow 1 uplift is marked by a gradual folding of strata (Figs 2B and C). The fold is a ~4.8 × 3.3 km, flat-topped dome with a monoclinal rim and covers a greater area than the underlying intrusion (Fig. 4B). The current maximum amplitude of the fold is ~120 ms TWT (~150–210 m) (Fig. 4B). In places, immediately overlying reflections onlap the folded Intra-Barrow 1 horizon (Fig. 2B). The reflection that marks the Intra-Barrow 1 horizon displays a positive polarity and has an overall moderate amplitude, although there is a 1–2 km wide zone where the reflection has a high amplitude

(Figs 2B, C, and 4B). This high amplitude zone trends north and is deflected around the fold (Fig. 3B). Between the Near Base Cretaceous unconformity and the Intra-Barrow 1 horizon there is a clear thickening of the stratal package (up to ~225 ms TWT, or ~281–393 m, thick) within the graben hosting the intrusion (Figs 2B, C, and 4C). A zone of marked thinning interrupts this thickening trend and coincides with the area of uplift above the intrusion; here the Near Base Cretaceous unconformity to Intra-Barrow 1 strata is $\lesssim$137 ms TWT ($\lesssim$171–239 m) thick (Fig. 4C). The NE-SW striking graben within the area of uplift hosts a thicker (~34–40 ms TWT, 42–70 m thick) succession of the Near Base Cretaceous unconformity to Intra-Barrow 1 strata compared to its flanks (Fig. 4C).

The Intra-Barrow 2 horizon corresponds to a moderate amplitude, positive polarity reflection that, like Intra-Barrow 1, displays little evidence of faulting and a prominent flat-topped fold (green horizon with black outline in Figs 2B, C, and 4D). The fold at Intra-Barrow 2 is ~5.0 × 3.5 km, larger than the fold area expressed at Intra-Barrow 1 and that of the intrusion, and its current maximum amplitude is ~150 ms TWT (~191–268 m) (Fig. 4D). Between the Intra-Barrow 1 and Intra-Barrow 2 horizons there is a gradual westward thickening of strata regionally (Figs 2B, C, and 4E). Across the fold, the strata bound by Intra-Barrow 1 and Intra-Barrow 2 locally thins to $\lesssim$50 ms TWT ($\lesssim$63–88 m), except where it thickens to ~100 ms TWT (~125–175 m) into the intra-fold graben expressed along the Near Base Cretaceous unconformity (Figs 2B, C, and 4E). Reflections immediately above the Intra-Barrow 2 horizon dip gently to the NE and correspond to the toesets of Barrow Group clinoforms (Figs 2B, C, and 4F). These clinoform reflections, including the Intra-Barrow 3 horizon, onlap onto the fold and are absent across the north-western part of the fold (Figs 2B, C, and 4F). Above the Intra-Barrow 3 horizon, younger clinoforms reflections that dip to the NE and cover the fold locally have inflection points that occur at structurally shallower levels than those beyond the fold limit (Figs 2B and C). The supra-intrusion fold is also expressed at the Top Barrow Group (green solid horizon), where it has a maximum amplitude of ~50 ms TWT (~63–88 m), up to the Top Muderong Shale (light green horizon), where its maximum amplitude is ~40 ms TWT (~50–70 m) (Figs 2B, C, 4G and I). A key observation is that with the exception of the Top Barrow Group, no reflections onlap onto the fold above the Intra-Barrow 2 horizon (Figs 2B and C); at the Top Barrow, overlying reflections do onlap onto the horizon but do so regionally, not just across the fold (Figs 2B and C). Strata between both the Intra-Barrow 2 and Top Barrow Group, as well as the Top Barrow Group to Top Muderong Shale, display subtle thinning across the fold, but around its immediate periphery there is a zone of local thickening (Figs 4H and J).

Discussion

The mapped intrusion is dominated by a tabular main body that is consistently ~261–319 m thick, except where a NE-trending ridge is developed along the top contact. The main body is encompassed by centrally dipping inclined sheets (Figs 2B, C, and 3). The intrusion is only ~4.5 km long (Fig. 3A) and thus has a length-to-thickness ratio of ~15, which suggests it can be defined as either a laccolith or sill (Cruden et al. 2017); given its greater thickness compared to previously identified sills offshore NW Australia (e.g., Magee et al., 2013a, b; Mark et al., 2020), we favour describing the intrusion as a laccolith. Given the spatial restriction of the dome-shaped fold above the laccolith, we consider it a forced fold that formed either (Fig. 5): (i) to make space for the intruding magma volume (Pollard & Johnson 1973; Hansen & Cartwright 2006; Jackson et al. 2013); and/or (ii) via later differential compaction as the porosity of the sedimentary strata adjacent to the laccolith gradually reduces during burial, whilst the thickness of the incompressible intrusion remains constant (Schmiedel et al. 2017; Magee et al. 2019). To determine the possible impact of intrusion-related deformation on surface morphology and sediment dispersal, we first need to establish how and when the forced fold developed (Smallwood & Maresh 2002; Magee et al. 2017a).

Folding mechanisms and timing

Deformation related to the laccolith appears to affect strata situated just above the Top Mungaroo Formation up to the Top Muderong Shale (Figs 2 and 4). In the lowermost section of this sedimentary sequence, below the Near Base Cretaceous unconformity, deformation is related to sub-vertical faults located along the laccolith edge (Figs 2B, C, and 3A). Similar relationships between tabular intrusions, faults, and overburden uplift are recognised in a variety of geological settings, as well as physical and numerical models, where deformation is driven by magma emplacement (de Saint-Blanquat et al. 2006; Magee et al. 2017a; Montanari et al. 2017). In contrast to strata below the Near Base Cretaceous unconformity, which are largely faulted, strata above this unconformity are primarily deformed by folding (Figs 2 and 4). At both the Intra-Barrow 1 and Intra-Barrow 2 horizons, we observe overlying reflections onlapping onto the fold (Figs 2B, C, 4E, and F), which indicates the surface was locally uplifted and deposition was restricted across its crest; i.e. the Intra-Barrow 1 and 2 horizons mark palaeosurfaces that were contemporaneous to a phase of fold development (Trude et al. 2003). We also note that within the folded strata, between the Intra-Barrow 1 horizon and the laccolith top, two graben-bounding normal faults and associated minor normal faults are developed (Figs 2B, C, and 4A). Although these normal faults within the fold are typically NE-trending and parallel to many of the large tectonic normal faults in the area, they do not extend beyond the fold limits (Fig. 4A). Similar normal faults have been observed in natural and modelled intrusion-induced forced folds, and occur in response to outer-arc extension generated during the bending of strata above intruding magma (Pollard & Johnson 1973; Magee et al. 2013b; Montanari et al. 2017). Based on the structure and seismic-stratigraphic relationships of the forced fold below the Intra-Barrow 2 horizon, and their similarity to intrusion-induced forced folds elsewhere, we suggest space for magma emplacement was, at least partly, generated by overburden uplift (Figs 5A, 6A, and B). Specifically, we suggest magma emplacement and folding began in the Early Cretaceous, when the Intra-Barrow 1 horizon represented the surface, and involved erosion of strata above the Near Base Cretaceous unconformity across its crest (Fig. 6A) (Trude et al. 2003); we suggest this erosion produced the observed thinning of the Near Base Cretaceous unconformity to Intra-Barrow 1 strata across the forced fold (Fig. 4C). We lack the data resolution to determine whether magma emplacement and folding occurred continuously up to when the Intra-Barrow 2 horizon marked the surface, or if their growth were incremental (Trude et al. 2003; Reeves et al. 2018). With laccolith inflation and continued folding, bending-related stresses likely instigated faulting around the intrusion periphery and fold crest, facilitating uplift and perhaps providing pathways for magma ascent and inclined sheet formation (Fig. 6B) (Pollard & Johnson 1973; Jackson & Pollard 1990; Thomson & Schofield 2008).

Above the Intra-Barrow 2 horizon, the forced fold is subtly expressed at several horizons up to the Top Muderong Shale (Figs 2B, C, and 4). Throughout the Intra-Barrow 2 to Top Muderong Shale succession, we only observe onlap onto the fold at the Top Barrow Group, but note this horizon is equivalent to a regional unconformity and onlap of overlying reflections also occurs regionally beyond the fold limits (Figs 2B and C). On thickness maps of the Intra-Barrow 2 to Top Barrow Group, as well as the Top Barrow Group to Top Muderong Shale, it is apparent that the strata thins across the fold and there is a zone of increased thickness encircling but beyond the fold periphery (Figs 4H and J). These thickening patterns and the lack of onlapping reflections local onto the forced fold are consistent with its formation via post-emplacement, differential compaction during burial (Figs 5B and 6C) (Hansen & Cartwright 2006; Jackson et al. 2013; Schmiedel et al. 2017).

Influence of intrusion-related ground deformation on the stratigraphic record

Having established that laccolith emplacement induced surface uplift in the Early Cretaceous, we now examine its effect on sedimentation patterns. First, the occurrence of onlapping reflections onto the forced fold at the Intra-Barrow 1 and Intra-Barrow 2 horizons demonstrates intrusion-induced uplift can locally restrict deposition (Figs 2B, C, and 4F). For example, the mapped distribution of the Intra-Barrow 3 horizon indicates the north-eastwards progradation of Barrow Group clinoforms were locally impeded by relief associated with the forced fold (Fig. 4F) (Reeve et al. 2016; Paumard et al. 2018). There is also a possible channel feature developed along the Intra-Barrow 1 horizon, expressed as a <2 km wide high amplitude zone, which appears to have been deflected around the forced fold (Figs 2B, C, and 4B). Overall, our results, coupled with observations of surface uplift at active volcanoes, demonstrate that ground deformation driven by magma emplacement can instigate abrupt changes in geomorphology and sediment dispersal, which may be modified over years to millions of years as intrusion (periodically) continues (Smallwood & Maresh 2002; Egbeni et al. 2014; Magee et al. 2014; Magee et al. 2017a; Reeves et al. 2018).

A key aspect of studying palaeosurface geomorphology with seismic reflection data is determining whether mapped horizons have been modified post-burial. Our work supports previous studies that show differential compaction of strata across an area hosting a solidified igneous intrusion can produce a forced fold, independent of magma emplacement (Hansen & Cartwright 2006; Jackson et al. 2013; Schmiedel et al. 2017). Importantly, we observe inflection points of the Barrow Group clinoforms to be situated at shallower structural levels within the forced fold compared to beyond its limit (Fig. 2B). If such differential compaction was not recognised or explicitly accounted for, variations in clinoform trajectory might erroneously be interpreted as evidence for changes in relative sea level; i.e., apparent rising trajectories on the landward side of the forced fold record sea-level rise, whereas falling trajectories on the seaward side record sea-level fall (e.g., Steel et al. 2002). Yet if we account for differential compaction by flattening the Top Barrow Group, we see that there is no local change in clinoform inflection trajectory (Fig. 7). Considering how differential compaction may affect subsurface structures in volcanic areas, where incompressible intrusive or extrusive igneous rocks occur, is critical to properly assessing palaeosurface geomorphology (Clairmont et al. 2021).

Conclusions

Unravelling how magma emplacement translates into ground deformation can help us evaluate potential volcanic hazards in areas where we cannot directly access the subsurface. As part of our endeavour to improve hazard assessment, we need to better understand how volcanic landforms evolve through time and interact with surface processes. Seismic reflection geomorphology offers an exciting opportunity to study active and ancient volcanic landforms in 3D. Here we use 3D seismic reflection data from offshore NW Australia to study a laccolith and overlying forced fold. By identifying seismic-stratigraphic onlap onto the forced fold we demonstrate magma emplacement instigated overburden uplift in the Early Cretaceous. Associated ground deformation restricted sediment deposition and deflected a channel within the overlying Barrow Group, a package of deep-water shelf margin clinoforms. With continued deposition and burial of the study area, differential compaction produced a forced fold on top of that generated by magma emplacement; i.e. strata adjacent to the laccolith were able to compact but the intrusion itself was relatively incompressible, limiting subsidence of the overlying sedimentary column. We demonstrate that differential compaction locally modified the relative position of clinoform inflection points, which if not recognised can be misinterpreted as a systems tract variation. Overall, our study serves to highlight the possible benefits and complications of seismic geomorphology in volcanic areas.

Acknowledgements

This study formed represents work conducted by ED during their MSci undergraduate project. The seismic and well data are open access and can be found through Geoscience Australia (www.ga.gov.au/nopims) to whom we are grateful. We also acknowledge Schlumberger for providing Petrel seismic interpretation software.

Figure captions

Figure 1: (A) Offshore NW Australia map showing key tectonic and basin elements (modified from Norcliffe et al. 2021). NCB = North Carnarvon Basin, SCB = South Carnarvon Basin, ExSB = Exmouth Sub-basin, BSB = Barrow Sub-basin, DSB = Dampier Sub-basin, PS = Peedamullah Shelf, WP = Wallaby Plateau, CAP = Cuvier Abyssal Plain, GAP = Gascoyne Abyssal Plain, AAP = Argo Abyssal Plain, CRFZ Cape Range Fracture Zone. Elevation data from the 2009 Australian Bathymetry and Topography grid (Geoscience Australia). (B) Stratigraphic column for the Exmouth Plateau highlighting important tectonic and magmatic events (based on Hocking et al. 1987; Hocking 1992; Tindale et al. 1998; Longley et al. 2002; Magee & Jackson 2020). (C) Uninterpreted and interpreted 2D seismic line across the Exmouth Plateau and Exmouth Sub-basin (Norcliffe et al. 2021). See (A) for location.

Figure 2: (A) Time-structure map of the Top Mungaroo Formation across the Glencoe 3D survey. Boreholes shown are 1 = Chester-1ST1, 2 = Warrior-1, 3 = Nimblefoot-1, 4 = Rimfire-1, 5 = Glencoe-1, 6 = Briseis-1. (B and C) Uninterpreted and interpreted seismic sections showing the structural and stratigraphic framework of the studied intrusion and fold. In (C) we show the synthetic well-tie between the seismic section and Chester-1ST1, which we created by using well-log (density RHOB; sonic velocity, DT) and checkshot data to produce a sonic calibration and time-depth relationship. A Ricker wavelet of 25 Hz was used to create the synthetic seismogram. TVD is true vertical depth (km) and TWT is two-way time (seconds). See (A) for locations.

Figure 3: Time-structure maps of the Top (A) and Base (B) Intrusion reflections, and a map of vertical intrusion thickness where both top and base reflections can be distinguished in the data (i.e. the main body of the intrusion).

Figure 4: Time-structure and thickness maps for the interpreted horizons. From the Intra-Barrow 1 horizon (B), we also show an RMS (Root-mean squared) amplitude map to highlight the presence of a possible channel.

Figure 5: Schematics showing the two end-member processes for forming forced folds above intrusions: (i) syn-emplacement uplift to generate space for the intruding magma (A); and (ii) post-emplacement differential compaction that occurs during burial of the sedimentary sequence (B) (modified from Magee et al. 2014).

Figure 6: Schematics showing our interpretation of laccolith emplacement and forced folding. (A) Sill emplacement and inflation in the first stage are spatially accommodated by

overburden uplift, but erosion of the contemporaneous surface (i.e. the Intra-Barrow 1 horizon) across the fold removes material. (B) In the second stage, after deposition of sediment onlapping onto the fold at the Intra-Barrow 1 horizon, continued or renewed magma emplacement and laccolith inflation drive further uplift. (C) The final phase of fold development occurs after magma emplacement ceases, whereby the sedimentary column adjacent to the laccolith compacts more than that above the intrusion (i.e. differential compaction).

Figure 7: Uninterpreted and interpreted seismic section shown in Figure 2B, but here we have flattened the data on the Top Barrow Group horizon to show the likely original clinoforms geometry. See Figure 2A for line location.

References

Bilal, A., McClay, K. & Scarselli, N. 2018. Fault-scarp degradation in the central Exmouth Plateau, North West Shelf, Australia. *Geological Society, London, Special Publications*, **476**, SP476. 411.

Brown, A.R. 2011. *Interpretation of three-dimensional seismic data*. 6th ed. AAPG and SEG, Oklahoma, USA.

Childs, K., Banfield, J., Jakymec, M. & Jones, A. 2013. *Well Completion Report: Chester-1 & Chester-1 ST1 interpretative data.* Hess.

Clairmont, R., Kolawole, F., Omale, A.P. & Bedle, H. 2021. Controls of pre-existing structures on clinoform architecture and the associated progradational system elements. *Basin Research*, **33**, 875-902.

Cruden, A., McCaffrey, K. & Bunger, A. 2017. Geometric scaling of tabular igneous intrusions: Implications for emplacement and growth.

de Saint-Blanquat, M., Habert, G., Horsman, E., Morgan, S.S., Tikoff, B., Launeau, P. & Gleizes, G. 2006. Mechanisms and duration of non-tectonically assisted magma emplacement in the upper crust: the Black Mesa pluton, Henry Mountains, Utah. *Tectonophysics,* **428**, 1-31.

Direen, N.G., Stagg, H.M.J., Symonds, P.A. & Colwell, J.B. 2008. Architecture of volcanic rifted margins: new insights from the Exmouth – Gascoyne margin, Western Australia. *Australian Journal of Earth Sciences*, **55**, 341-363.

Egbeni, S., McClay, K., Jian-kui Fu, J. & Bruce, D. 2014. Influence of igneous sills on Paleocene turbidite deposition in the Faroe–Shetland Basin: a case study in Flett and Muckle sub-basin and its implication for hydrocarbon exploration. *Geological Society, London, Special Publications*, **397**, 33-57, http://doi.org/10.1144/sp397.8.

Exon, N., Von Rad, U. & Von Stackelberg, U. 1982. The geological development of the passive margins of the Exmouth Plateau off northwest Australia. *Marine Geology*, **47**, 131-152.

Exon, N., Haq, B. & Von Rad, U. 1992. Exmouth Plateau revisited: scientific drilling and geological framework. *Proceedings of the Ocean Drilling Program, Scientific Results*, 3-20.

Frey, Ø., Planke, S., Symonds, P.A. & Heeremans, M. 1998. Deep crustal structure and rheology of the Gascoyne volcanic margin, western Australia. *Marine Geophysical Researches*, **20**, 293-311.

Galland, O. & Scheibert, J. 2013. Analytical model of surface uplift above axisymmetric flat-lying magma intrusions: Implications for sill emplacement and geodesy. *Journal of Volcanology and Geothermal Research*, **253**, 114-130.

Gibbons, A.D., Barckhausen, U., den Bogaard, P., Hoernle, K., Werner, R., Whittaker, J.M. & Müller, R.D. 2012. Constraining the Jurassic extent of Greater India: Tectonic evolution of the West Australian margin. *Geochemistry, Geophysics, Geosystems*, **13**, Q05W13.

Hansen, D.M. & Cartwright, J. 2006. The three-dimensional geometry and growth of forced folds above saucer-shaped igneous sills. *Journal of Structural Geology*, **28**, 1520-1535.

Hocking, R. 1992. Jurassic deposition in the southern and central North West Shelf. *Western Australia: Geological Survey Western Australia Record*, **199217**.

Hocking, R.M., Moors, H.T. & Van de Graaff, W.E. 1987. *Geology of the carnarvon basin, Western Australia*. State Print. Division.

Hopper, J.R., Mutter, J.C., Larson, R.L. & Mutter, C.Z. 1992. Magmatism and rift margin evolution: Evidence from northwest Australia. *Geology*, **20**, 853-857.

Jackson, C.A.-L., Schofield, N. & Golenkov, B. 2013. Geometry and controls on the development of igneous sill–related forced folds: A 2-D seismic reflection case study from offshore southern Australia. *Geological Society of America Bulletin*, **125**, 1874-1890.

Jackson, M.D. & Pollard, D.D. 1990. Flexure and faulting of sedimentary host rocks during growth of igneous domes, Henry Mountains, Utah. *Journal of Structural Geology*, **12**, 185-206.

Karlstrom, L., Richardson, P.W., O'Hara, D. & Ebmeier, S.K. 2018. Magmatic landscape construction. *Journal of Geophysical Research: Earth Surface*, **123**, 1710-1730.

Longley, I., Buessenschuett, C., Clydsdale, L., Cubitt, C., Davis, R., Johnson, M., Marshall, N., Murray, A., *et al.* 2002. The North West Shelf of Australia–a Woodside perspective. *The sedimentary basins of Western Australia*, **3**, 27-88.

Magee, C. & Jackson, C.-L. 2020. Seismic reflection data reveal the 3D structure of the newly discovered Exmouth Dyke Swarm, offshore NW Australia. *Solid Earth*, **11**, 576-606.

Magee, C., Jackson, C.A.-L. & Schofield, N. 2013a. The influence of normal fault geometry on igneous sill emplacement and morphology. *Geology*, **41**, 407-410.

Magee, C., Briggs, F. & Jackson, C.A.-L. 2013b. Lithological controls on igneous intrusion-induced ground deformation. *Journal of the Geological Society*, **170**, 853-856.

Magee, C., Jackson, C.L. & Schofield, N. 2014. Diachronous sub-volcanic intrusion along deep-water margins: insights from the Irish Rockall Basin. *Basin Research*, **26**, 85-105.

Magee, C., Maharaj, S.M., Wrona, T. & Jackson, C.A.-L. 2015. Controls on the expression of igneous intrusions in seismic reflection data. *Geosphere*, **11**, 1024-1041.

Magee, C., Jackson, C.A.-L., Hardman, J.P. & Reeve, M.T. 2017a. Decoding sill emplacement and forced fold growth in the Exmouth Sub-basin, offshore northwest Australia: Implications for hydrocarbon exploration. *Interpretation*, **5**, SK11-SK22.

Magee, C., Hoggett, M., Jackson, C.A.-L. & Jones, S.M. 2019. Burial-Related Compaction Modifies Intrusion-Induced Forced Folds: Implications for Reconciling Roof Uplift Mechanisms Using Seismic Reflection Data. *Frontiers in Earth Science*, **7,** 37.

Magee, C., Bastow, I.D., de Vries, B.v.W., Jackson, C.A.-L., Hetherington, R., Hagos, M. & Hoggett, M. 2017b. Structure and dynamics of surface uplift induced by incremental sill emplacement. *Geology*, **45**, 431-434.

Mark, N., Holford, S.P., Schofield, N., Eide, C.H., Pugliese, S., Watson, D. & Muirhead, D. 2020. Structural and lithological controls on the architecture of igneous intrusions: examples from the NW Australian Shelf. *Petroleum Geoscience,* **26**, 50-69.

Moig N & Massie, S. 2010. *Well Completion Report, Rimfire-1, Interpretative data.* Hess Exploration Australia Pty Limited.

Montanari, D., Bonini, M., Corti, G., Agostini, A., Del Ventisette, C.J.J.o.V. & Research, G. 2017. Forced folding above shallow magma intrusions: Insights on supercritical fluid flow from analogue modelling. **345**, 67-80.

Norcliffe, J., Magee, C., Jackson, C., Kopping, J. & Lathrop, B. 2021. Fault inversion contributes to ground deformation above inflating igneous sills. *Volcanica*, **4**, 1-21.

Paumard, V., Bourget, J., Payenberg, T., Ainsworth, R.B., George, A.D., Lang, S., Posamentier, H.W. & Peyrot, D. 2018. Controls on shelf-margin architecture and sediment partitioning during a syn-rift to post-rift transition: Insights from the Barrow Group (Northern Carnarvon Basin, North West Shelf, Australia). *Earth-Science Reviews*, **177**, 643-677.

Planke, S., Rasmussen, T., Rey, S.S. & Myklebust, R. 2005. Seismic characteristics and distribution of volcanic intrusions and hydrothermal vent complexes in the Vøring and Møre basins. *In*: Doré, A.G. (ed) *Petroleum Geology: North-West Europe and Global Perspectives - Proceddings of the 6th Petroleum Geology Conference*. Geological Society, London, 833-844.

Pollard, D.D. & Johnson, A.M. 1973. Mechanics of growth of some laccolithic intrusions in the Henry Mountains, Utah, II: bending and failure of overburden layers and sill formation. *Tectonophysics*, **18**, 311-354.

Reeve, M.T., Jackson, C.A.L., Bell, R.E., Magee, C. & Bastow, I.D. 2016. The stratigraphic record of prebreakup geodynamics: Evidence from the Barrow Delta, offshore Northwest Australia. *Tectonics*, **35**, 1935-1968.

Reeve, M.T., Magee, C., Bastow, I.D., McDermott, C., Jackson, C.A.-L., Bell, R.E. & Prytulak, J. 2021. Nature of the Cuvier Abyssal Plain crust, offshore NW Australia. *Journal of the Geological Society*.

Reeves, J., Magee, C. & Jackson, C.A.L. 2018. Unravelling intrusion-induced forced fold kinematics and ground deformation using 3D seismic reflection data. *Volcanica*, **1**, 1-17.

Rey, S.S., Planke, S., Symonds, P.A. & Faleide, J.I. 2008. Seismic volcanostratigraphy of the Gascoyne margin, Western Australia. *Journal of Volcanology and Geothermal Research*, **172**, 112-131.

Rohrman, M. 2013. Intrusive large igneous provinces below sedimentary basins: An example from the Exmouth Plateau (NW Australia). *Journal of Geophysical Research: Solid Earth*, **118**, 4477-4487.

Rohrman, M. 2015. Delineating the Exmouth mantle plume (NW Australia) from denudation and magmatic addition estimates. *Lithosphere*, L445. 441.

Schmiedel, T., Kjoberg, S., Planke, S., Magee, C., Galland, O., Schofield, N., Jackson, C.A.-L. & Jerram, D.A. 2017. Mechanisms of overburden deformation associated with the emplacement of the Tulipan sill, mid-Norwegian margin. *Interpretation*, **5**, SK23-SK38.

Segall, P. 2013. Volcano deformation and eruption forecasting. *Geological Society, London, Special Publications*, **380**.

Skogly, O. 1998. *Seismic characterization and emplacement of intrusives in the Vøring Basin.* M.Sc. Thesis, University of Oslo.

Smallwood, J.R. & Maresh, J. 2002. The properties, morphology and distribution of igneous sills: modelling, borehole data and 3D seismic from the Faroe-Shetland area. *In*: Jolley, D.W. & Bell, B.R. (eds) *The North Atlantic Igneous Province: Stratigraphy, tectonic, Volcanic and Magmatic Processes*. Geological Society, London, Special Publications, **197**, 271-306.

Stagg, H., Alcock, M., Bernardel, G., Moore, A., Symonds, P. & Exon, N. 2004. *Geological framework of the outer Exmouth Plateau and adjacent ocean basins*. Geoscience Australia.

Steel, R., Olsen, T., Armentrout, J. & Rosen, N. 2002. Clinoforms, clinoform trajectories and deepwater sands. *Sequence-stratigraphic models for exploration and production: Evolving methodology, emerging models and application histories: Gulf Coast Section SEPM 22nd Research Conference, Houston, Texas*, 367-381.

Symonds, P.A., Planke, S., Frey, O. & Skogseid, J. 1998. Volcanic evolution of the Western Australian Continental Margin and its implications for basin development. *The Sedimentary Basins of Western Australia 2: Proc. of Petroleum Society Australia Symposium, Perth, WA*.

Thomson, K. & Schofield, N. 2008. Lithological and structural controls on the emplacement and morphology of sills in sedimentary basins. *In*: Thomson, K. & Petford, N. (eds) *Structure and Emplacement of High-Level Magmatic Systems*. Geological Society, London, Special Publications, **302**, 31-44.

Tindale, K., Newell, N., Keall, J. & Smith, N. 1998. Structural evolution and charge history of the Exmouth Sub-basin, northern Carnarvon Basin, Western Australia. *The Sedimentary Basins of Western Australia 2: Proc. of Petroleum Society Australia Symposium, Perth, WA*, 473-490.

Trude, J., Cartwright, J., Davies, R.J. & Smallwood, J.R. 2003. New technique for dating igneous sills. *Geology*, **31**, 4.

van Wyk de Vries, B., Márquez, A., Herrera, R., Bruña, J.G., Llanes, P. & Delcamp, A. 2014. Craters of elevation revisited: forced-folds, bulging and uplift of volcanoes. *Bulletin of Volcanology*, **76**, 1-20.

Widess, M. 1973. How thin is a thin bed? *Geophysics*, **38**, 1176-1180.

Willcox, J. & Exon, N.J.T.A.J. 1976. The regional geology of the Exmouth Plateau. **16**, 1-11.

Figure 1

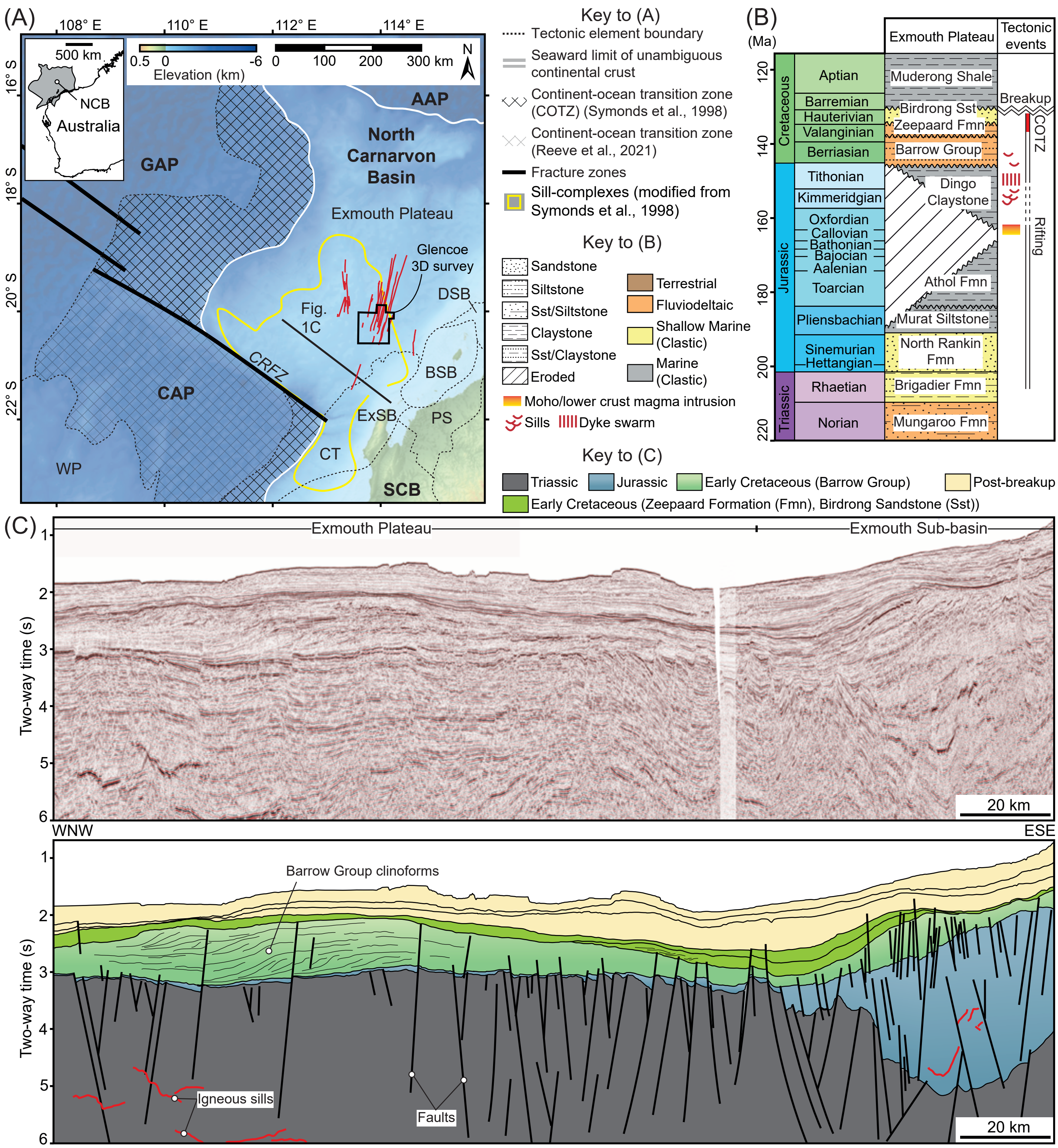

(A)
108° E
110° E
112° E
114° E
16° S
18° S
20° S
22° S
500 km
NCB
Australia
0.5 0 -6
Elevation (km)
0 100 200 300 km
N
AAP
GAP
North Carnarvon Basin
Exmouth Plateau
Glencoe 3D survey
Fig. 1C
DSB
CRFZ
BSB
CAP
ExSB
PS
CT
WP
SCB
Key to (A)
Tectonic element boundary
Seaward limit of unambiguous continental crust
Continent-ocean transition zone (COTZ) (Symonds et al., 1998)
Continent-ocean transition zone (Reeve et al., 2021)
Fracture zones
Sill-complexes (modified from Symonds et al., 1998)
Key to (B)
Sandstone
Siltstone
Sst/Siltstone
Claystone
Sst/Claystone
Eroded
Terrestrial
Fluviodeltaic
Shallow Marine (Clastic)
Marine (Clastic)
Moho/lower crust magma intrusion
Sills
Dyke swarm
Key to (C)
Triassic
Jurassic
Early Cretaceous (Barrow Group)
Post-breakup
Early Cretaceous (Zeepaard Formation (Fmn), Birdrong Sandstone (Sst))
(B)
(Ma)
Exmouth Plateau
Tectonic events
120
140
160
180
200
220
Cretaceous
Jurassic
Triassic
Aptian
Barremian
Hauterivian
Valanginian
Berriasian
Tithonian
Kimmeridgian
Oxfordian
Callovian
Bathonian
Bajocian
Aalenian
Toarcian
Pliensbachian
Sinemurian
Hettangian
Rhaetian
Norian
Muderong Shale
Birdrong Sst
Zeepaard Fmn
Barrow Group
Dingo Claystone
Athol Fmn
Murat Siltstone
North Rankin Fmn
Brigadier Fmn
Mungaroo Fmn
Breakup
COTZ
Rifting
(C)
Exmouth Plateau
Exmouth Sub-basin
Two-way time (s)
1
2
3
4
5
6
20 km
WNW
ESE
Barrow Group clinoforms
Igneous sills
Faults

Figure 2

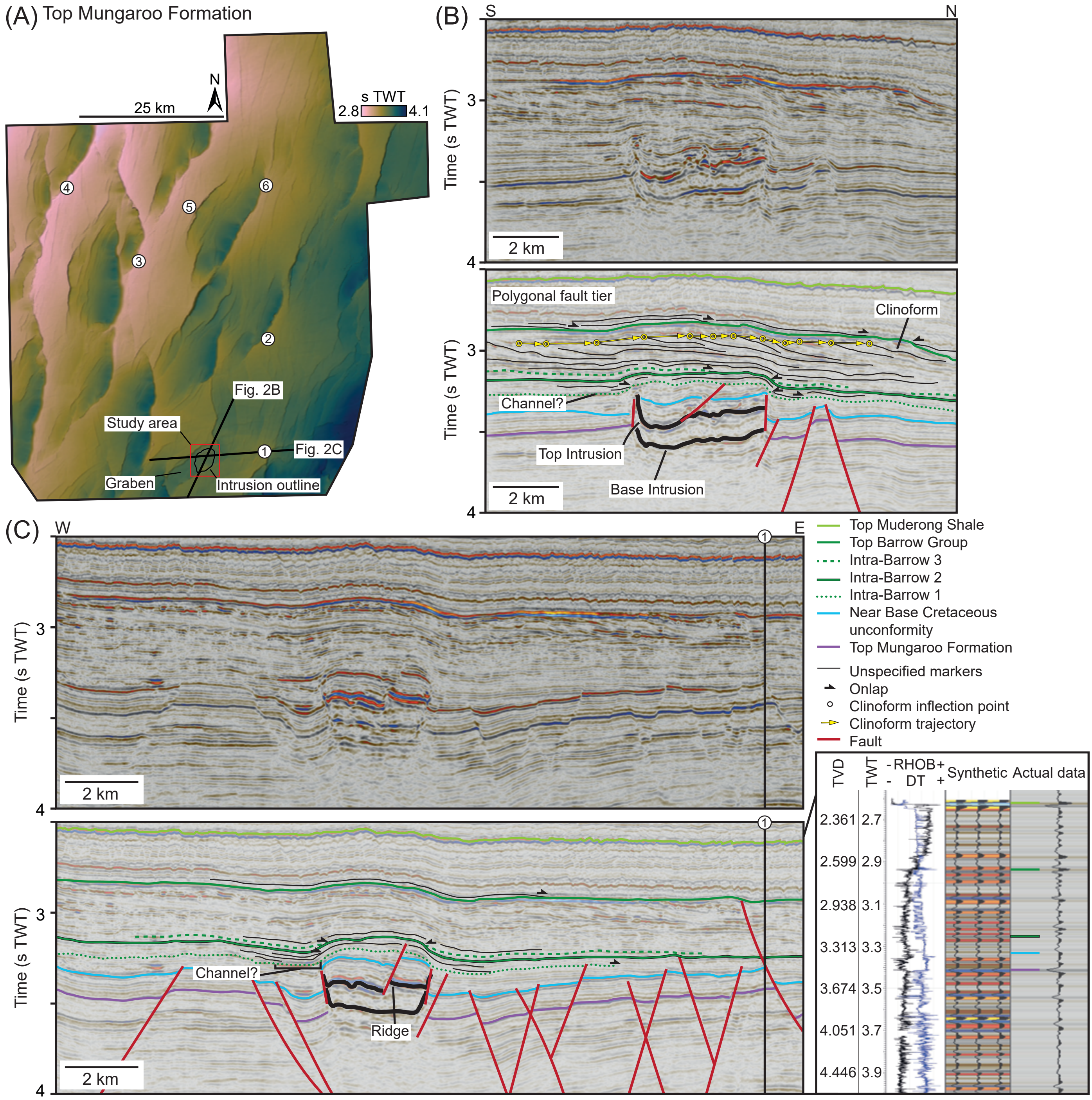

(A) Top Mungaroo Formation
N
25 km
s TWT
2.8
4.1
1
2
3
4
5
6
Fig. 2B
Fig. 2C
Study area
Graben
Intrusion outline
(B)
S
N
Time (s TWT)
3
4
2 km
Polygonal fault tier
Clinoform
Channel?
Top Intrusion
Base Intrusion
(C)
W
E
Ridge
Top Muderong Shale
Top Barrow Group
Intra-Barrow 3
Intra-Barrow 2
Intra-Barrow 1
Near Base Cretaceous unconformity
Top Mungaroo Formation
Unspecified markers
Onlap
Clinoform inflection point
Clinoform trajectory
Fault
TVD
TWT
- RHOB +
- DT +
Synthetic
Actual data
2.361 2.7
2.599 2.9
2.938 3.1
3.313 3.3
3.674 3.5
4.051 3.7
4.446 3.9

Figure 3

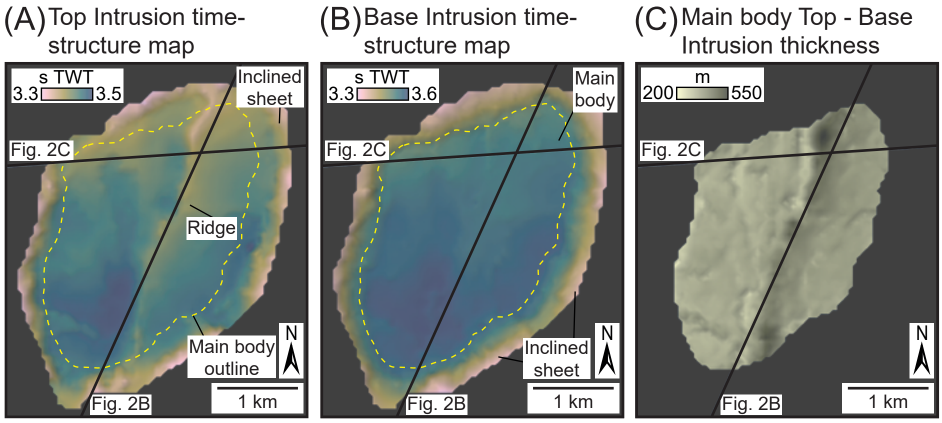

(A) Top Intrusion time-structure map
s TWT
3.3
3.5
Inclined sheet
Fig. 2C
Ridge
Main body outline
N
Fig. 2B
1 km
(B) Base Intrusion time-structure map
s TWT
3.3
3.6
Main body
Fig. 2C
Inclined sheet
N
Fig. 2B
1 km
(C) Main body Top - Base Intrusion thickness
m
200
550
Fig. 2C
N
Fig. 2B
1 km

Figure 4

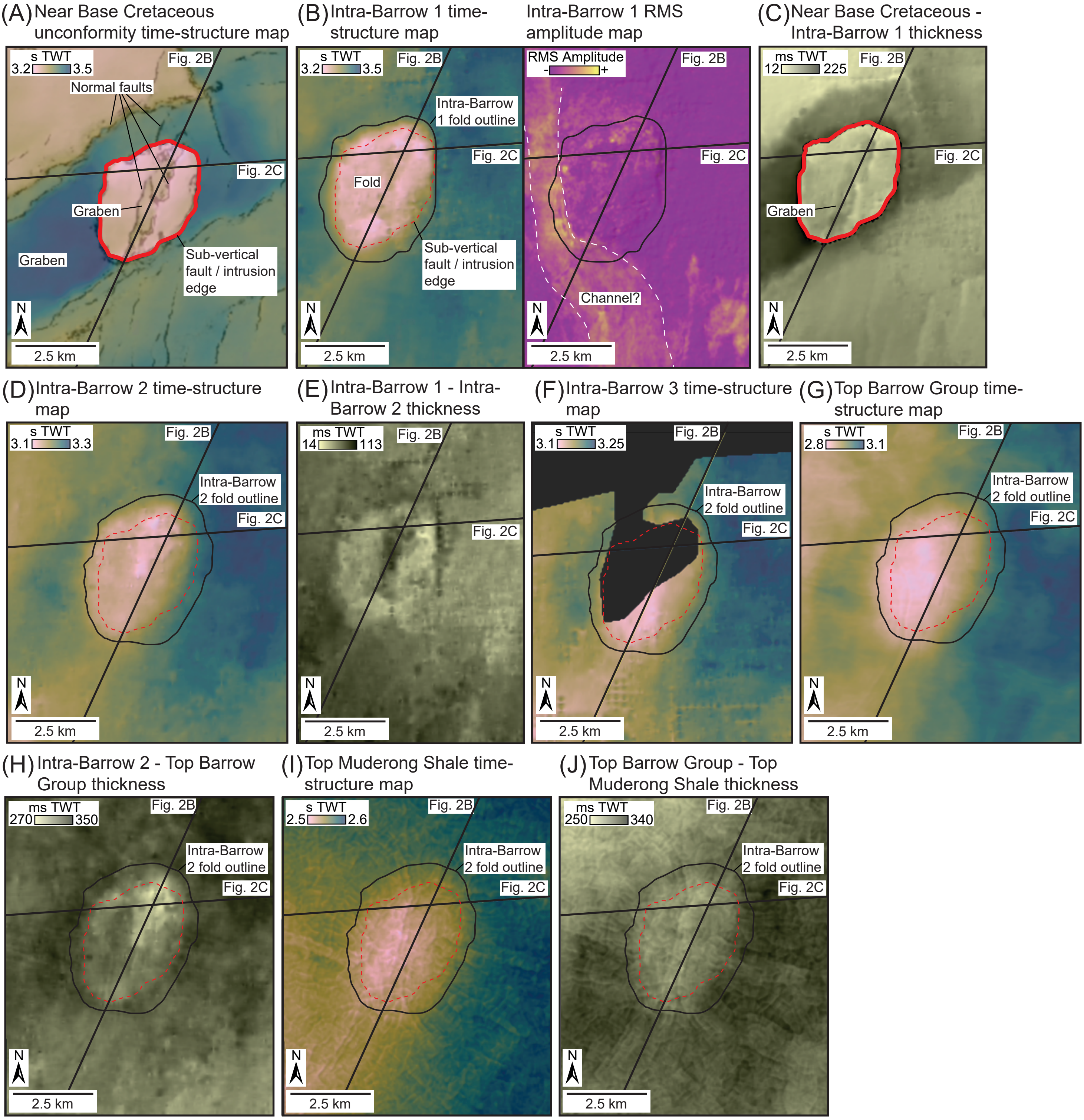
(A) Near Base Cretaceous unconformity time-structure map
s TWT
3.2
3.5
Fig. 2B
Normal faults
Fig. 2C
Graben
Graben
Sub-vertical fault / intrusion edge
N
2.5 km
(B) Intra-Barrow 1 time-structure map
s TWT
3.2
3.5
Fig. 2B
Intra-Barrow 1 fold outline
Fig. 2C
Fold
Sub-vertical fault / intrusion edge
N
2.5 km
Intra-Barrow 1 RMS amplitude map
RMS Amplitude
-
+
Fig. 2B
Fig. 2C
Channel?
N
2.5 km
(C) Near Base Cretaceous - Intra-Barrow 1 thickness
ms TWT
12
225
Fig. 2B
Fig. 2C
Graben
N
2.5 km
(D) Intra-Barrow 2 time-structure map
s TWT
3.1
3.3
Fig. 2B
Intra-Barrow 2 fold outline
Fig. 2C
N
2.5 km
(E) Intra-Barrow 1 - Intra-Barrow 2 thickness
ms TWT
14
113
Fig. 2B
Fig. 2C
N
2.5 km
(F) Intra-Barrow 3 time-structure map
s TWT
3.1
3.25
Fig. 2B
Intra-Barrow 2 fold outline
Fig. 2C
N
2.5 km
(G) Top Barrow Group time-structure map
s TWT
2.8
3.1
Fig. 2B
Intra-Barrow 2 fold outline
Fig. 2C
N
2.5 km
(H) Intra-Barrow 2 - Top Barrow Group thickness
ms TWT
270
350
Fig. 2B
Intra-Barrow 2 fold outline
Fig. 2C
N
2.5 km
(I) Top Muderong Shale time-structure map
s TWT
2.5
2.6
Fig. 2B
Intra-Barrow 2 fold outline
Fig. 2C
N
2.5 km
(J) Top Barrow Group - Top Muderong Shale thickness
ms TWT
250
340
Fig. 2B
Intra-Barrow 2 fold outline
Fig. 2C
N
2.5 km

Figure 5

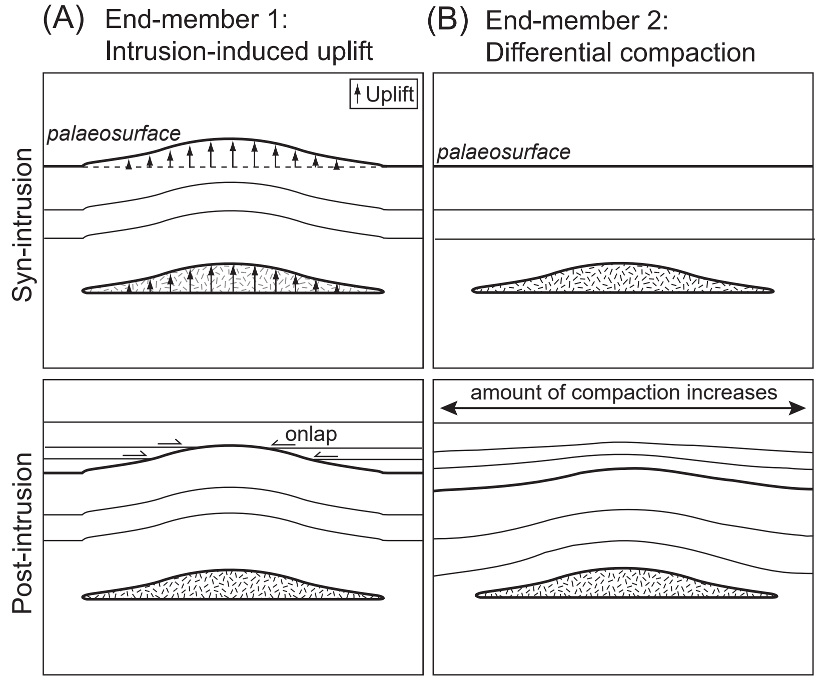
(A) End-member 1: Intrusion-induced uplift
(B) End-member 2: Differential compaction
Uplift
palaeosurface
palaeosurface
Syn-intrusion
Post-intrusion
amount of compaction increases
onlap

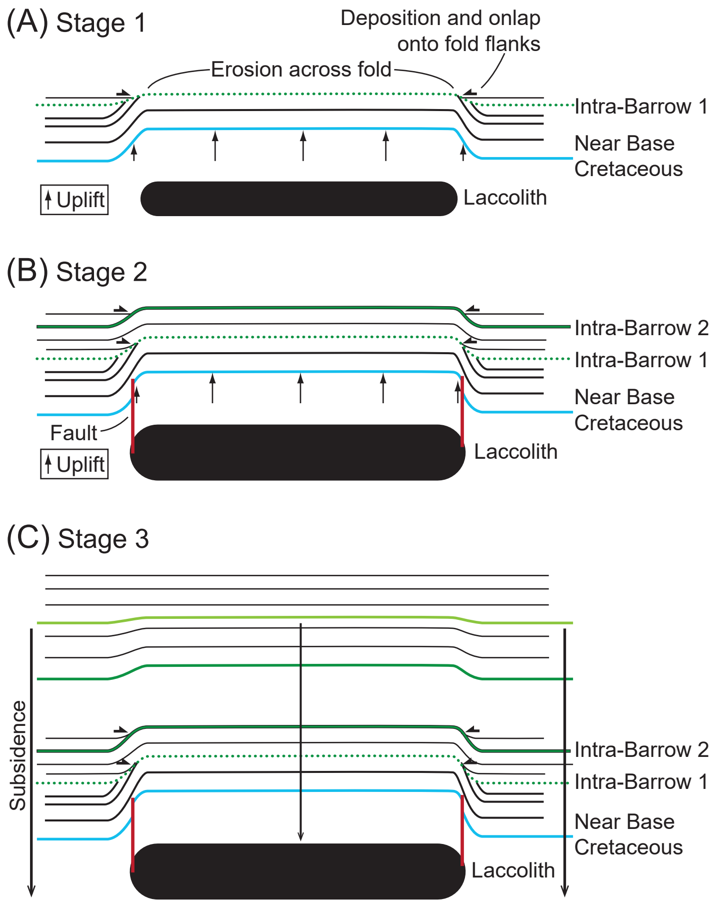

(A) Stage 1
Deposition and onlap onto fold flanks
Erosion across fold
Intra-Barrow 1
Near Base Cretaceous
Uplift
Laccolith
(B) Stage 2
Intra-Barrow 2
Intra-Barrow 1
Near Base Cretaceous
Fault
Uplift
Laccolith
(C) Stage 3
Subsidence
Intra-Barrow 2
Intra-Barrow 1
Near Base Cretaceous
Laccolith

Figure 7

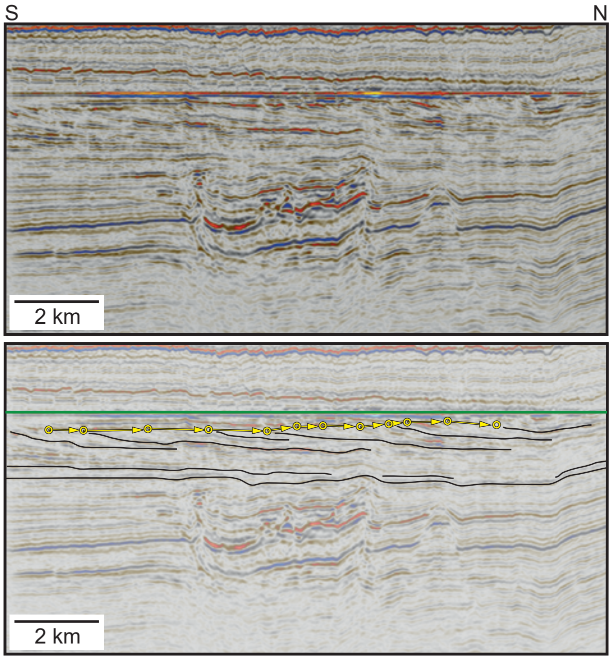

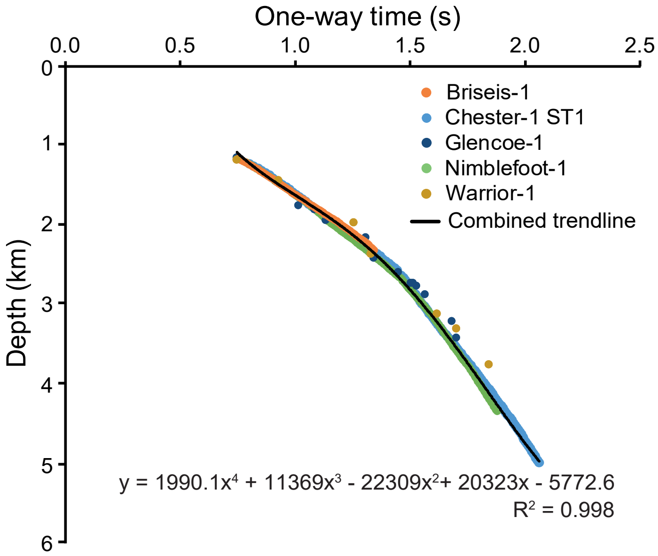

Supplementary Figure 1: Time-depth data for the five wells used in the study. Fitting a fourh-order polynomial trend-line through the cumulative data, and extrapolating it downwards, allows us to define seismic velocities at any depth.

Supplementary Table 1: Well checkshot data

Briseis-1			Chester-1 ST1			Glencoe-1			Nimblefoot-1			
Two-way Time [TWT] (s)	One-way Time [OWT] (s)	Measured depth [MD] (m)	Two-way Time [TWT] (s)	One-way Time [OWT] (s)	Measured depth [MD] (m)	Two-way Time [TWT] (s)	One-way Time [OWT] (s)	Measured depth [MD] (m)	Two-way Time [TWT] (s)	One-way Time [OWT] (s)	Measured depth [MD] (m)	Two-way Time [TWT] (s)
1.520	0.760	1166.2	1.595	0.797	1225.0	1.500	0.750	1150.2	1.582	0.791	1214.5	1.500
1.540	0.770	1181.3	1.630	0.815	1255.0	2.035	1.018	1749.0	1.602	0.801	1229.1	1.860
1.558	0.779	1196.4	1.667	0.834	1285.0	2.172	1.086	1798.3	1.621	0.810	1244.3	2.510
1.579	0.789	1211.5	1.700	0.850	1315.0	2.272	1.136	1939.5	1.639	0.819	1259.4	2.660
1.597	0.799	1226.7	1.735	0.868	1345.0	2.616	1.308	2149.5	1.657	0.828	1274.5	3.230
1.615	0.808	1241.8	1.767	0.883	1375.0	2.684	1.342	2405.5	1.674	0.837	1289.2	3.400
1.634	0.817	1256.8	1.798	0.899	1405.0	2.900	1.450	2585.0	1.691	0.845	1304.3	3.680
1.651	0.825	1271.9	1.824	0.912	1435.0	3.004	1.502	2721.5	1.707	0.854	1319.4	
1.670	0.835	1287.1	1.851	0.925	1465.0	3.024	1.512	2721.5	1.723	0.861	1334.5	
1.687	0.844	1302.2	1.881	0.940	1495.0	3.056	1.528	2756.8	1.737	0.868	1349.2	
1.705	0.852	1317.0	1.913	0.957	1525.0	3.129	1.565	2868.5	1.753	0.876	1364.3	
1.721	0.861	1332.1	1.941	0.971	1555.0	3.363	1.682	3201.0	1.768	0.884	1379.4	
1.738	0.869	1347.3	1.972	0.986	1585.0	3.400	1.700	3410.0	1.784	0.892	1394.5	
1.753	0.877	1362.4	1.999	0.999	1615.0				1.800	0.900	1409.2	
1.768	0.884	1377.6	2.027	1.014	1645.0				1.817	0.908	1424.3	
1.783	0.892	1392.7	2.055	1.028	1675.0				1.832	0.916	1439.4	
1.799	0.900	1407.8	2.083	1.042	1705.0				1.847	0.923	1454.5	
1.815	0.907	1423.0	2.110	1.055	1735.0				1.861	0.931	1469.0	
1.832	0.916	1438.3	2.139	1.070	1765.0				1.877	0.938	1484.1	
1.848	0.924	1453.4	2.167	1.084	1795.0				1.891	0.946	1499.2	
1.863	0.932	1468.5	2.196	1.098	1825.0				1.905	0.953	1514.4	
1.878	0.939	1483.6	2.224	1.112	1855.0				1.919	0.960	1529.1	
1.892	0.946	1498.8	2.253	1.126	1885.0				1.935	0.967	1544.3	
1.906	0.953	1514.0	2.285	1.142	1915.0				1.949	0.975	1559.4	
1.920	0.960	1529.1	2.315	1.158	1945.0				1.964	0.982	1574.5	
1.934	0.967	1544.2	2.345	1.173	1975.0				1.978	0.989	1589.2	
1.949	0.975	1559.2	2.375	1.188	2005.0				1.993	0.997	1604.3	
1.964	0.982	1574.4	2.406	1.203	2035.0				2.009	1.004	1619.4	
1.980	0.990	1589.5	2.435	1.218	2065.0				2.024	1.012	1634.5	
1.995	0.998	1604.6	2.464	1.232	2095.0				2.039	1.019	1649.1	
2.012	1.006	1619.7	2.491	1.246	2125.0				2.053	1.027	1664.3	
2.028	1.014	1634.8	2.517	1.258	2155.0				2.069	1.034	1679.4	
2.044	1.022	1649.9	2.542	1.271	2185.0				2.083	1.042	1694.5	
2.059	1.030	1665.0	2.570	1.285	2215.0				2.099	1.049	1709.2	
2.076	1.038	1680.2	2.598	1.299	2245.0				2.114	1.057	1724.3	
2.093	1.047	1695.3	2.676	1.338	2335.0				2.127	1.064	1739.4	
2.108	1.054	1710.5	2.703	1.352	2365.0				2.140	1.070	1754.5	
2.123	1.062	1725.6	2.730	1.365	2395.0				2.152	1.076	1769.2	
2.138	1.069	1740.7	2.756	1.378	2425.0				2.165	1.082	1784.3	
2.155	1.077	1755.8	2.782	1.391	2455.0				2.177	1.089	1799.4	
2.171	1.086	1771.0	2.807	1.403	2485.0				2.189	1.095	1814.5	
2.187	1.094	1786.1	2.832	1.416	2515.0				2.202	1.101	1829.2	
2.204	1.102	1801.2	2.856	1.428	2545.0				2.214	1.107	1844.3	

2.222	1.111	1816.3
2.236	1.118	1831.5
2.252	1.126	1846.6
2.268	1.134	1861.6
2.283	1.142	1876.7
2.301	1.150	1891.8
2.316	1.158	1907.0
2.334	1.167	1922.1
2.351	1.176	1937.2
2.367	1.184	1952.3
2.382	1.191	1967.5
2.396	1.198	1982.5
2.409	1.205	1997.6
2.422	1.211	2012.8
2.437	1.219	2027.9
2.451	1.226	2043.1
2.466	1.233	2058.2
2.481	1.240	2073.4
2.495	1.247	2088.5
2.508	1.254	2103.6
2.524	1.262	2118.7
2.538	1.269	2133.9
2.551	1.276	2149.0
2.565	1.283	2164.2
2.580	1.290	2179.3
2.595	1.297	2194.4
2.609	1.305	2209.5
2.623	1.311	2224.6
2.635	1.317	2239.7
2.646	1.323	2254.8
2.657	1.329	2269.9
2.668	1.334	2285.0
2.680	1.340	2300.1
2.692	1.346	2315.2

2.878	1.439	2575.0
2.916	1.458	2635.0
2.934	1.467	2665.0
2.950	1.475	2695.0
2.964	1.482	2725.0
2.979	1.490	2755.0
2.994	1.497	2785.0
3.007	1.504	2815.0
3.022	1.511	2845.0
3.037	1.519	2875.0
3.052	1.526	2905.0
3.067	1.534	2935.0
3.083	1.542	2965.0
3.099	1.550	2995.0
3.115	1.557	3025.0
3.130	1.565	3055.0
3.146	1.573	3085.0
3.161	1.581	3115.0
3.177	1.589	3145.0
3.193	1.597	3175.0
3.209	1.604	3205.0
3.224	1.612	3235.0
3.240	1.620	3265.0
3.256	1.628	3295.0
3.272	1.636	3325.0
3.288	1.644	3355.0
3.306	1.653	3385.0
3.324	1.662	3415.0
3.342	1.671	3445.0
3.359	1.679	3475.0
3.375	1.687	3505.0
3.390	1.695	3535.0
3.405	1.702	3565.0
3.422	1.711	3595.0
3.439	1.719	3625.0
3.455	1.728	3655.0
3.471	1.736	3685.0
3.488	1.744	3715.0
3.505	1.753	3745.0
3.522	1.761	3775.0
3.539	1.769	3805.0
3.555	1.778	3835.0
3.571	1.786	3865.0
3.587	1.793	3895.0
3.602	1.801	3925.0
3.618	1.809	3955.0
3.634	1.817	3985.0
3.650	1.825	4015.0
3.666	1.833	4045.0

2.225	1.113	1859.4
2.237	1.118	1874.5
2.247	1.124	1889.2
2.259	1.130	1904.3
2.271	1.136	1919.4
2.284	1.142	1934.5
2.298	1.149	1949.1
2.295	1.147	1949.2
2.312	1.156	1964.3
2.309	1.154	1964.3
2.325	1.163	1979.4
2.322	1.161	1979.4
2.338	1.169	1994.5
2.334	1.167	1994.5
2.349	1.175	2009.1
2.363	1.181	2024.3
2.377	1.188	2039.4
2.390	1.195	2054.5
2.403	1.201	2069.2
2.417	1.209	2084.3
2.432	1.216	2099.4
2.446	1.223	2114.5
2.460	1.230	2129.1
2.474	1.237	2144.3
2.489	1.244	2159.4
2.503	1.251	2174.5
2.516	1.258	2189.1
2.530	1.265	2204.3
2.543	1.271	2219.4
2.556	1.278	2234.5
2.569	1.284	2249.1
2.582	1.291	2264.3
2.596	1.298	2279.4
2.609	1.305	2294.5
2.622	1.311	2309.1
2.635	1.317	2324.3
2.648	1.324	2339.4
2.661	1.330	2354.5
2.673	1.337	2369.2
2.686	1.343	2384.3
2.699	1.350	2399.4
2.712	1.356	2414.5
2.725	1.362	2429.2
2.738	1.369	2444.3
2.750	1.375	2459.4
2.763	1.381	2474.5
2.775	1.388	2489.1
2.788	1.394	2504.3
2.801	1.401	2519.4

3.682	1.841	4075.0
3.697	1.848	4105.0
3.711	1.856	4135.0
3.727	1.863	4165.0
3.742	1.871	4195.0
3.757	1.878	4225.0
3.772	1.886	4255.0
3.787	1.894	4285.0
3.803	1.901	4315.0
3.818	1.909	4345.0
3.833	1.917	4375.0
3.848	1.924	4405.0
3.864	1.932	4435.0
3.878	1.939	4465.0
3.893	1.946	4495.0
3.907	1.954	4525.0
3.921	1.961	4555.0
3.935	1.968	4585.0
3.949	1.975	4615.0
3.962	1.981	4645.0
3.976	1.988	4675.0
3.988	1.994	4705.0
4.002	2.001	4735.0
4.015	2.008	4765.0
4.029	2.014	4795.0
4.043	2.021	4825.0
4.056	2.028	4855.0
4.069	2.034	4885.0
4.080	2.040	4915.0
4.090	2.045	4945.0
4.103	2.051	4975.0
4.116	2.058	5005.0

2.814	1.407	2534.5
2.826	1.413	2549.2
2.838	1.419	2564.3
2.851	1.425	2579.4
2.863	1.431	2594.5
2.873	1.436	2609.1
2.875	1.438	2609.2
2.885	1.442	2624.2
2.887	1.443	2624.3
2.896	1.448	2639.4
2.898	1.449	2639.4
2.908	1.454	2654.5
2.910	1.455	2654.5
2.921	1.460	2669.1
2.930	1.465	2684.3
2.940	1.470	2699.4
2.950	1.475	2714.5
2.957	1.479	2729.1
2.965	1.482	2744.3
2.973	1.486	2759.4
2.981	1.490	2774.5
2.988	1.494	2789.1
2.998	1.499	2804.3
3.007	1.503	2819.4
3.017	1.509	2834.5
3.025	1.512	2849.2
3.034	1.517	2864.3
3.044	1.522	2879.4
3.053	1.527	2894.5
3.061	1.531	2909.2
3.071	1.535	2924.3
3.081	1.540	2939.4
3.088	1.544	2954.5
3.097	1.548	2969.1
3.107	1.553	2984.2
3.117	1.559	2999.3
3.125	1.562	3014.5
3.134	1.567	3029.1
3.142	1.571	3044.2
3.151	1.575	3059.4
3.159	1.580	3074.5
3.167	1.583	3089.1
3.176	1.588	3104.2
3.184	1.592	3119.3
3.192	1.596	3134.5
3.201	1.600	3149.1
3.209	1.604	3164.2
3.216	1.608	3179.3
3.223	1.612	3194.5

3.230	1.615	3209.1
3.239	1.619	3224.2
3.245	1.622	3239.3
3.252	1.626	3254.5
3.259	1.629	3269.1
3.266	1.633	3284.3
3.273	1.637	3299.4
3.280	1.640	3314.5
3.287	1.643	3329.1
3.294	1.647	3344.2
3.302	1.651	3359.4
3.308	1.654	3374.5
3.315	1.658	3389.1
3.324	1.662	3404.3
3.330	1.665	3419.4
3.337	1.669	3434.5
3.344	1.672	3449.1
3.351	1.676	3464.3
3.359	1.679	3479.4
3.365	1.683	3494.5
3.372	1.686	3509.1
3.378	1.689	3524.3
3.386	1.693	3539.4
3.394	1.697	3554.5
3.402	1.701	3569.2
3.410	1.705	3584.3
3.417	1.708	3599.4
3.425	1.712	3614.5
3.432	1.716	3629.1
3.440	1.720	3644.3
3.447	1.724	3659.4
3.454	1.727	3674.5
3.462	1.731	3689.1
3.470	1.735	3704.2
3.478	1.739	3719.3
3.487	1.744	3734.4
3.497	1.748	3749.1
3.504	1.752	3764.2
3.512	1.756	3779.4
3.519	1.759	3794.5
3.526	1.763	3809.1
3.533	1.767	3824.2
3.540	1.770	3839.3
3.546	1.773	3854.5
3.552	1.776	3869.1
3.559	1.779	3884.2
3.565	1.782	3899.3
3.571	1.786	3914.5
3.578	1.789	3929.1

3.584	1.792	3944.2
3.591	1.796	3959.4
3.598	1.799	3974.5
3.605	1.803	3989.1
3.612	1.806	4004.2
3.619	1.809	4019.4
3.625	1.812	4034.5
3.630	1.815	4049.1
3.638	1.819	4064.3
3.644	1.822	4079.4
3.650	1.825	4094.5
3.657	1.829	4109.1
3.664	1.832	4124.2
3.670	1.835	4139.3
3.676	1.838	4154.5
3.682	1.841	4169.1
3.689	1.845	4184.3
3.695	1.848	4199.4
3.702	1.851	4214.5
3.708	1.854	4229.1
3.716	1.858	4244.2
3.722	1.861	4259.4
3.729	1.865	4274.5
3.736	1.868	4289.2
3.743	1.871	4304.3
3.749	1.875	4319.4
3.756	1.878	4334.6

Warrior-1		All data		
One-way Time [OWT] (s)	Measured depth [MD] (m)	Two-way Time [TWT] (s)	One-way Time [OWT] (s)	Measured depth [MD] (m)
0.750	1172.1	1.520	0.760	1166.2
0.930	1429.2	1.540	0.770	1181.3
1.255	1959.6	1.558	0.779	1196.4
1.330	2356.5	1.579	0.789	1211.5
1.615	3106.0	1.597	0.799	1226.7
1.700	3293.2	1.615	0.808	1241.8
1.840	3748.0	1.634	0.817	1256.8
		1.651	0.825	1271.9
		1.670	0.835	1287.1
		1.687	0.844	1302.2
		1.705	0.852	1317.0
		1.721	0.861	1332.1
		1.738	0.869	1347.3
		1.753	0.877	1362.4
		1.768	0.884	1377.6
		1.783	0.892	1392.7
		1.799	0.900	1407.8
		1.815	0.907	1423.0
		1.832	0.916	1438.3
		1.848	0.924	1453.4
		1.863	0.932	1468.5
		1.878	0.939	1483.6
		1.892	0.946	1498.8
		1.906	0.953	1514.0
		1.920	0.960	1529.1
		1.934	0.967	1544.2
		1.949	0.975	1559.2
		1.964	0.982	1574.4
		1.980	0.990	1589.5
		1.995	0.998	1604.6
		2.012	1.006	1619.7
		2.028	1.014	1634.8
		2.044	1.022	1649.9
		2.059	1.030	1665.0
		2.076	1.038	1680.2
		2.093	1.047	1695.3
		2.108	1.054	1710.5
		2.123	1.062	1725.6
		2.138	1.069	1740.7
		2.155	1.077	1755.8
		2.171	1.086	1771.0
		2.187	1.094	1786.1
		2.204	1.102	1801.2

2.222	1.111	1816.3
2.236	1.118	1831.5
2.252	1.126	1846.6
2.268	1.134	1861.6
2.283	1.142	1876.7
2.301	1.150	1891.8
2.316	1.158	1907.0
2.334	1.167	1922.1
2.351	1.176	1937.2
2.367	1.184	1952.3
2.382	1.191	1967.5
2.396	1.198	1982.5
2.409	1.205	1997.6
2.422	1.211	2012.8
2.437	1.219	2027.9
2.451	1.226	2043.1
2.466	1.233	2058.2
2.481	1.240	2073.4
2.495	1.247	2088.5
2.508	1.254	2103.6
2.524	1.262	2118.7
2.538	1.269	2133.9
2.551	1.276	2149.0
2.565	1.283	2164.2
2.580	1.290	2179.3
2.595	1.297	2194.4
2.609	1.305	2209.5
2.623	1.311	2224.6
2.635	1.317	2239.7
2.646	1.323	2254.8
2.657	1.329	2269.9
2.668	1.334	2285.0
2.680	1.340	2300.1
2.692	1.346	2315.2
1.595	0.797	1225.0
1.630	0.815	1255.0
1.667	0.834	1285.0
1.700	0.850	1315.0
1.735	0.868	1345.0
1.767	0.883	1375.0
1.798	0.899	1405.0
1.824	0.912	1435.0
1.851	0.925	1465.0
1.881	0.940	1495.0
1.913	0.957	1525.0
1.941	0.971	1555.0
1.972	0.986	1585.0
1.999	0.999	1615.0
2.027	1.014	1645.0

2.055	1.028	1675.0
2.083	1.042	1705.0
2.110	1.055	1735.0
2.139	1.070	1765.0
2.167	1.084	1795.0
2.196	1.098	1825.0
2.224	1.112	1855.0
2.253	1.126	1885.0
2.285	1.142	1915.0
2.315	1.158	1945.0
2.345	1.173	1975.0
2.375	1.188	2005.0
2.406	1.203	2035.0
2.435	1.218	2065.0
2.464	1.232	2095.0
2.491	1.246	2125.0
2.517	1.258	2155.0
2.542	1.271	2185.0
2.570	1.285	2215.0
2.598	1.299	2245.0
2.676	1.338	2335.0
2.703	1.352	2365.0
2.730	1.365	2395.0
2.756	1.378	2425.0
2.782	1.391	2455.0
2.807	1.403	2485.0
2.832	1.416	2515.0
2.856	1.428	2545.0
2.878	1.439	2575.0
2.916	1.458	2635.0
2.934	1.467	2665.0
2.950	1.475	2695.0
2.964	1.482	2725.0
2.979	1.490	2755.0
2.994	1.497	2785.0
3.007	1.504	2815.0
3.022	1.511	2845.0
3.037	1.519	2875.0
3.052	1.526	2905.0
3.067	1.534	2935.0
3.083	1.542	2965.0
3.099	1.550	2995.0
3.115	1.557	3025.0
3.130	1.565	3055.0
3.146	1.573	3085.0
3.161	1.581	3115.0
3.177	1.589	3145.0
3.193	1.597	3175.0
3.209	1.604	3205.0

3.224	1.612	3235.0
3.240	1.620	3265.0
3.256	1.628	3295.0
3.272	1.636	3325.0
3.288	1.644	3355.0
3.306	1.653	3385.0
3.324	1.662	3415.0
3.342	1.671	3445.0
3.359	1.679	3475.0
3.375	1.687	3505.0
3.390	1.695	3535.0
3.405	1.702	3565.0
3.422	1.711	3595.0
3.439	1.719	3625.0
3.455	1.728	3655.0
3.471	1.736	3685.0
3.488	1.744	3715.0
3.505	1.753	3745.0
3.522	1.761	3775.0
3.539	1.769	3805.0
3.555	1.778	3835.0
3.571	1.786	3865.0
3.587	1.793	3895.0
3.602	1.801	3925.0
3.618	1.809	3955.0
3.634	1.817	3985.0
3.650	1.825	4015.0
3.666	1.833	4045.0
3.682	1.841	4075.0
3.697	1.848	4105.0
3.711	1.856	4135.0
3.727	1.863	4165.0
3.742	1.871	4195.0
3.757	1.878	4225.0
3.772	1.886	4255.0
3.787	1.894	4285.0
3.803	1.901	4315.0
3.818	1.909	4345.0
3.833	1.917	4375.0
3.848	1.924	4405.0
3.864	1.932	4435.0
3.878	1.939	4465.0
3.893	1.946	4495.0
3.907	1.954	4525.0
3.921	1.961	4555.0
3.935	1.968	4585.0
3.949	1.975	4615.0
3.962	1.981	4645.0
3.976	1.988	4675.0

3.988	1.994	4705.0
4.002	2.001	4735.0
4.015	2.008	4765.0
4.029	2.014	4795.0
4.043	2.021	4825.0
4.056	2.028	4855.0
4.069	2.034	4885.0
4.080	2.040	4915.0
4.090	2.045	4945.0
4.103	2.051	4975.0
4.116	2.058	5005.0
1.500	0.750	1150.2
2.035	1.018	1749.0
2.172	1.086	1798.3
2.272	1.136	1939.5
2.616	1.308	2149.5
2.684	1.342	2405.5
2.900	1.450	2585.0
3.004	1.502	2721.5
3.024	1.512	2721.5
3.056	1.528	2756.8
3.129	1.565	2868.5
3.363	1.682	3201.0
3.400	1.700	3410.0
1.582	0.791	1214.5
1.602	0.801	1229.1
1.621	0.810	1244.3
1.639	0.819	1259.4
1.657	0.828	1274.5
1.674	0.837	1289.2
1.691	0.845	1304.3
1.707	0.854	1319.4
1.723	0.861	1334.5
1.737	0.868	1349.2
1.753	0.876	1364.3
1.768	0.884	1379.4
1.784	0.892	1394.5
1.800	0.900	1409.2
1.817	0.908	1424.3
1.832	0.916	1439.4
1.847	0.923	1454.5
1.861	0.931	1469.0
1.877	0.938	1484.1
1.891	0.946	1499.2
1.905	0.953	1514.4
1.919	0.960	1529.1
1.935	0.967	1544.3
1.949	0.975	1559.4
1.964	0.982	1574.5

1.978	0.989	1589.2
1.993	0.997	1604.3
2.009	1.004	1619.4
2.024	1.012	1634.5
2.039	1.019	1649.1
2.053	1.027	1664.3
2.069	1.034	1679.4
2.083	1.042	1694.5
2.099	1.049	1709.2
2.114	1.057	1724.3
2.127	1.064	1739.4
2.140	1.070	1754.5
2.152	1.076	1769.2
2.165	1.082	1784.3
2.177	1.089	1799.4
2.189	1.095	1814.5
2.202	1.101	1829.2
2.214	1.107	1844.3
2.225	1.113	1859.4
2.237	1.118	1874.5
2.247	1.124	1889.2
2.259	1.130	1904.3
2.271	1.136	1919.4
2.284	1.142	1934.5
2.298	1.149	1949.1
2.295	1.147	1949.2
2.312	1.156	1964.3
2.309	1.154	1964.3
2.325	1.163	1979.4
2.322	1.161	1979.4
2.338	1.169	1994.5
2.334	1.167	1994.5
2.349	1.175	2009.1
2.363	1.181	2024.3
2.377	1.188	2039.4
2.390	1.195	2054.5
2.403	1.201	2069.2
2.417	1.209	2084.3
2.432	1.216	2099.4
2.446	1.223	2114.5
2.460	1.230	2129.1
2.474	1.237	2144.3
2.489	1.244	2159.4
2.503	1.251	2174.5
2.516	1.258	2189.1
2.530	1.265	2204.3
2.543	1.271	2219.4
2.556	1.278	2234.5
2.569	1.284	2249.1

2.582	1.291	2264.3
2.596	1.298	2279.4
2.609	1.305	2294.5
2.622	1.311	2309.1
2.635	1.317	2324.3
2.648	1.324	2339.4
2.661	1.330	2354.5
2.673	1.337	2369.2
2.686	1.343	2384.3
2.699	1.350	2399.4
2.712	1.356	2414.5
2.725	1.362	2429.2
2.738	1.369	2444.3
2.750	1.375	2459.4
2.763	1.381	2474.5
2.775	1.388	2489.1
2.788	1.394	2504.3
2.801	1.401	2519.4
2.814	1.407	2534.5
2.826	1.413	2549.2
2.838	1.419	2564.3
2.851	1.425	2579.4
2.863	1.431	2594.5
2.873	1.436	2609.1
2.875	1.438	2609.2
2.885	1.442	2624.2
2.887	1.443	2624.3
2.896	1.448	2639.4
2.898	1.449	2639.4
2.908	1.454	2654.5
2.910	1.455	2654.5
2.921	1.460	2669.1
2.930	1.465	2684.3
2.940	1.470	2699.4
2.950	1.475	2714.5
2.957	1.479	2729.1
2.965	1.482	2744.3
2.973	1.486	2759.4
2.981	1.490	2774.5
2.988	1.494	2789.1
2.998	1.499	2804.3
3.007	1.503	2819.4
3.017	1.509	2834.5
3.025	1.512	2849.2
3.034	1.517	2864.3
3.044	1.522	2879.4
3.053	1.527	2894.5
3.061	1.531	2909.2
3.071	1.535	2924.3

3.081	1.540	2939.4
3.088	1.544	2954.5
3.097	1.548	2969.1
3.107	1.553	2984.2
3.117	1.559	2999.3
3.125	1.562	3014.5
3.134	1.567	3029.1
3.142	1.571	3044.2
3.151	1.575	3059.4
3.159	1.580	3074.5
3.167	1.583	3089.1
3.176	1.588	3104.2
3.184	1.592	3119.3
3.192	1.596	3134.5
3.201	1.600	3149.1
3.209	1.604	3164.2
3.216	1.608	3179.3
3.223	1.612	3194.5
3.230	1.615	3209.1
3.239	1.619	3224.2
3.245	1.622	3239.3
3.252	1.626	3254.5
3.259	1.629	3269.1
3.266	1.633	3284.3
3.273	1.637	3299.4
3.280	1.640	3314.5
3.287	1.643	3329.1
3.294	1.647	3344.2
3.302	1.651	3359.4
3.308	1.654	3374.5
3.315	1.658	3389.1
3.324	1.662	3404.3
3.330	1.665	3419.4
3.337	1.669	3434.5
3.344	1.672	3449.1
3.351	1.676	3464.3
3.359	1.679	3479.4
3.365	1.683	3494.5
3.372	1.686	3509.1
3.378	1.689	3524.3
3.386	1.693	3539.4
3.394	1.697	3554.5
3.402	1.701	3569.2
3.410	1.705	3584.3
3.417	1.708	3599.4
3.425	1.712	3614.5
3.432	1.716	3629.1
3.440	1.720	3644.3
3.447	1.724	3659.4

3.454	1.727	3674.5
3.462	1.731	3689.1
3.470	1.735	3704.2
3.478	1.739	3719.3
3.487	1.744	3734.4
3.497	1.748	3749.1
3.504	1.752	3764.2
3.512	1.756	3779.4
3.519	1.759	3794.5
3.526	1.763	3809.1
3.533	1.767	3824.2
3.540	1.770	3839.3
3.546	1.773	3854.5
3.552	1.776	3869.1
3.559	1.779	3884.2
3.565	1.782	3899.3
3.571	1.786	3914.5
3.578	1.789	3929.1
3.584	1.792	3944.2
3.591	1.796	3959.4
3.598	1.799	3974.5
3.605	1.803	3989.1
3.612	1.806	4004.2
3.619	1.809	4019.4
3.625	1.812	4034.5
3.630	1.815	4049.1
3.638	1.819	4064.3
3.644	1.822	4079.4
3.650	1.825	4094.5
3.657	1.829	4109.1
3.664	1.832	4124.2
3.670	1.835	4139.3
3.676	1.838	4154.5
3.682	1.841	4169.1
3.689	1.845	4184.3
3.695	1.848	4199.4
3.702	1.851	4214.5
3.708	1.854	4229.1
3.716	1.858	4244.2
3.722	1.861	4259.4
3.729	1.865	4274.5
3.736	1.868	4289.2
3.743	1.871	4304.3
3.749	1.875	4319.4
3.756	1.878	4334.6
1.500	0.750	1172.1
1.860	0.930	1429.2
2.510	1.255	1959.6
2.660	1.330	2356.5

3.230	1.615	3106.0
3.400	1.700	3293.2
3.680	1.840	3748.0